Toward 4D Noise-Based Seismic Probing of Volcanoes: Perspectives from a Large-N Experiment on Piton de la Fournaise Volcano

by F. Brenguier, P. Kowalski, N. Ackerley, N. Nakata, P. Boué, M. Campillo, E. Larose, S. Rambaud, C. Pequegnat, T. Lecocq, P. Roux, V. Ferrazzini, N. Villeneuve, N. M. Shapiro, and J. Chaput

ABSTRACT

Noise-based seismology is proving to be a complementary approach to active-source or earthquake-based methods for imaging and monitoring the Earth's interior. Until recently, however, noise-based imaging and monitoring relied mostly on the inversion of surface waves reconstructed from correlations of mostly microseismic seismic noise (around 5 s of period). Compared to body-wave tomography and considering similar wavelengths, surface-wave tomography succeeds in retrieving lateral subsurface velocity contrasts but is less efficient in resolving velocity perturbations at depth. Recently, the use of large-*N* seismic arrays has proven to be of great benefit for extracting body waves from noise correlations by stacking over a large number of receiver pairs and by applying array processing. In this article, we describe a recent large-*N* array experiment that we conducted on Piton de la Fournaise (PdF). Our main goal was to extract body waves traveling directly in the vicinity of the active magma reservoir located at ~2.5 km depth below the summit crater using noise correlations between arrays of seismic sensors. Within this article, we provide technical information about the VolcArray experiment, which consisted of the deployment of 300 seismic nodes during one month on PdF. We also present data-quality measurements and show how the short-period seismometers that we used compare to standard broadband seismic records. Finally, we show noise array beamforming results to study the content of seismic noise at frequencies between 1 and 12 Hz and discuss the ability to use these data to recover body waves between arrays from the correlation of ambient seismic noise.

INTRODUCTION

Noise-based seismology is proving to be a complementary approach to active-source or earthquake-based methods for imaging and monitoring the Earth's interior. In particular, surface waves reconstructed from noise correlations have been used to image the crust from regional (Shapiro *et al.*, 2005) to local scales, including volcanoes (Brenguier *et al.*, 2007; Jaxybulatov *et al.*, 2014) and fault zones (Roux *et al.*, 2011). Noise-based seismology has also proven to be able to resolve subtle changes of the subsurface, opening the way to 4D probing of active faults and volcanoes (Sens-Schönfelder and Wegler, 2006; Brenguier *et al.*, 2008, 2014). Until recently, noise-based imaging and monitoring relied mostly on the inversion of surface-waves reconstructed from correlations of mostly microseismic seismic noise (around 5 s of period).

Compared to body-wave tomography and considering similar wavelengths, surface-wave tomography succeeds in retrieving lateral subsurface velocity contrasts but is less efficient in resolving velocity perturbations at depth. Moreover reflected body waves can carry direct information about sharp interfaces at depth. The study of Roux *et al.* (2005) showed that it was possible to extract direct diving *P* waves between sensors from noise correlations at a local scale. Also, recently, Nakata *et al.* (2015) were able to obtain a 3D body-wave tomography of the subsurface from correlations of seismic noise recorded at a dense array of more than 2500 seismic sensors in the city of Long Beach near Los Angeles. The use of large-*N* seismic arrays has proven to be of great benefit for extracting body waves from noise correlations by stacking over a large number of receiver pairs and by applying array processing.

Piton de la Fournaise volcano (PdF, La Réunion island) is a very active basaltic volcano, with one eruption per year on average. PdF is among the best-instrumented volcanoes worldwide, making it effectively a laboratory volcano for developing novel imaging and monitoring geophysical techniques. From 2009 to 2012, we conducted a dense broadband seismic experiment on PdF with the purpose of improving the spatial and temporal resolution of noise-based seismic monitoring of PdF's

doi: 10.1785/0220150173

eruptions (UnderVolc seismic experiment, Brenguier *et al.*, 2012). During the UnderVolc experiment, 21 broadband stations (separated by a few kilometers) were deployed. This high density of stations allowed us to reach a temporal resolution of noise-based seismic velocity changes of one day and a spatial lateral resolution of a few kilometers (Obermann *et al.*, 2013). For these studies, mostly surface waves reconstructed from correlations of noise at periods around 5 s are used. These studies were limited by the fact that, by using surface waves, (1) the spatial resolution at depth is poor and (2) seismic velocity changes measurements are hampered by near-surface effects such as rainfall-induced seismic velocity drops (Rivet *et al.*, 2015). To circumvent these issues, we conducted a large-*N* array experiment on PdF called VolcArray. Our main goal was to extract body waves traveling directly in the vicinity of the active magma reservoir located at ~2.5 km depth below the summit crater (Fig. 1) using noise correlations between arrays of seismic sensors.

Within this article, we will provide technical information about the VolcArray experiment, which consisted of the deployment of 300 seismic nodes during one month on PdF. We will also present data quality measurements from a noise spectral analysis using the IRIS-PASSCAL Quick Look eXtended tool (PQLX; McNamara and Buland, 2004) and coherence techniques, and we show how the short-period seismometers that we used compare to standard broadband seismic records. Finally, we will show noise-array beamforming results to study the content of seismic noise at frequencies between 1 and 12 Hz and discuss the ability to use these data to recover body waves between arrays from the correlation of ambient seismic noise.

THE EXPERIMENT

Array-type seismic experiments require the deployment of a large number of seismic sensors in a short amount of time. For this purpose, we used the technology of nodes that combine a geophone, digitizer, battery, data storage, and Global Positioning System in a single box (Hand, 2014). This easy-to-install system allowed us to deploy 300 nodes on the rough terrain of PdF volcano in 12 hr. Each node was composed of a vertical geophone of lower corner frequency 10 Hz and recorded data at a rate of 250 samples per second. Each array was composed of 7 × 7 grid points, in which each grid point was composed of two collocated seismic nodes (Fig. 1). The name of each grid point is composed of one alphabet and two digits referencing to lines and rows to identify the location within each array. For example, A12 is a grid point of array A on the first line and the second row. Line numbers increase from north to south, and row numbers increase from west to east. Each node was emplaced directly on the ground, without protection against wind or temperature changes. The purpose of deploying two collocated nodes was to acquire data for one month in total at each array grid point using seismic nodes

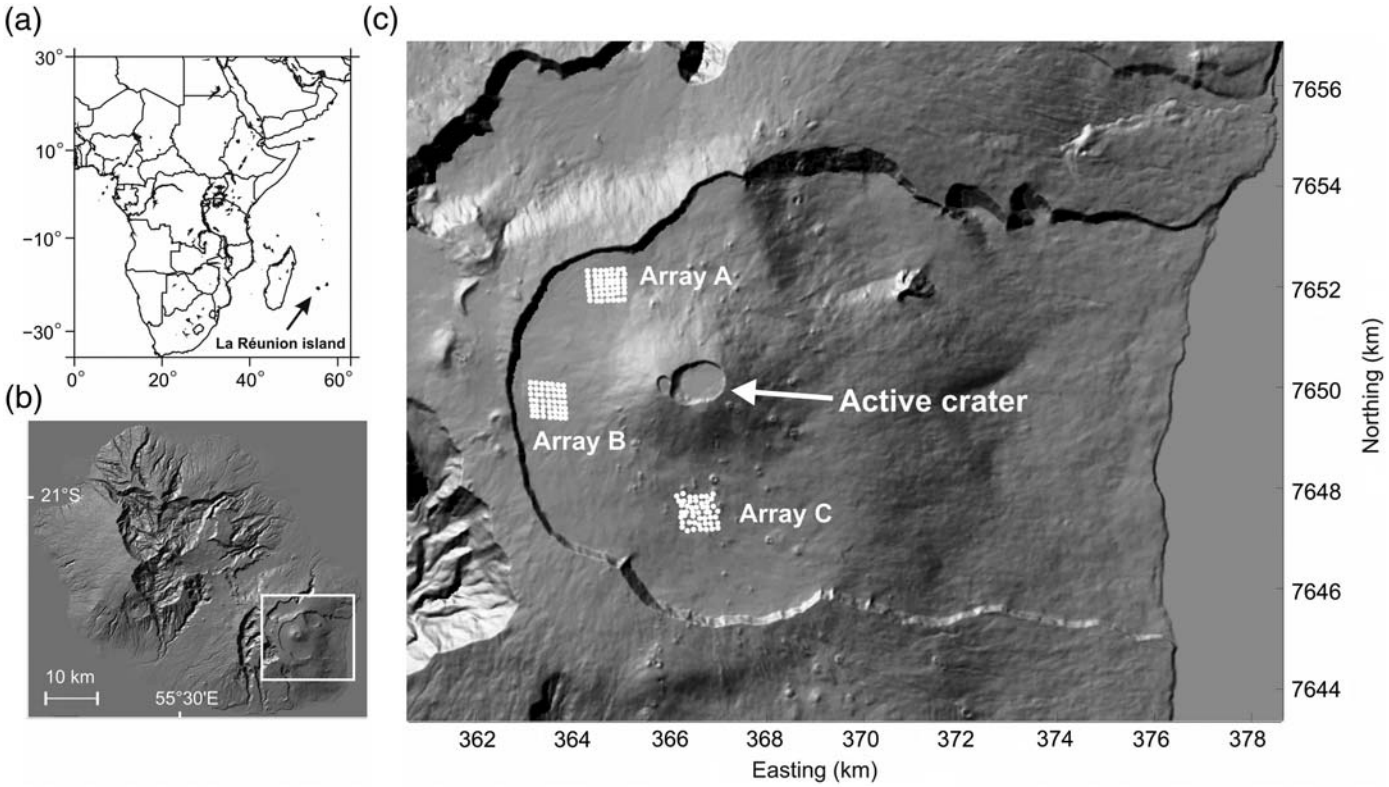

▲ **Figure 1.** Location of (a) La Réunion island, (b) Piton de la Fournaise volcano, and (c) the three seismic arrays. The CSS broadband seismic station is located inside array B.

with a battery life of, at minimum, 15 days. The time of acquisition of data for each series of seismic nodes is summarized in Figure 2. We found that the time intervals of data acquisition for the two sets of nodes overlapped, which proved to be very useful for assessing the quality of the data using coherence estimates from collocated nodes. The nodes were collected in two days and gathered to a central acquisition system to extract the raw data. The raw data in a proprietary format were converted to miniSEED format using a Python code available at https://github.com/ThomasLecocq/Fairfield-Receiver-Gather (last accessed October 2015), which uses functions of ObsPy (Beyreuther *et al.*, 2010).

SEISMIC DATA QUALITY OVERVIEW

For an overview of data quality, we computed power spectral density (PSD) probability density functions using PQLX (McNamara and Buland, 2004). The broadband station CSS of the Observatoire Volcanologique du Piton de la Fournaise was included, because it is located within array B, closest to station B33. The results for stations CSS, XP.B33.10, and XP.B33.20 are shown in Figure 3. Figure 3 shows that the data divides neatly into four bands. Below 0.1 Hz, the PSD is much higher in the XP network than at CSS because it is dominated by instrumental noise. Between 0.1 and 1 Hz, the PSD are very similar in the XP network and at CSS. Because this is an island site, the PSD of ground motion at the microseismic peak is quite high and thus can be clearly resolved by geophones. It is near 1 Hz where the ground motion most consistently exceeds the new high-noise model of Peterson (1993), which represented the maximum observed ground-motion PSD from a collection of 75 high-quality installations. Between 1 Hz and approximately 10 Hz, the noise levels are still similar in the XP network and at CSS; this is important, because it is close to the band of

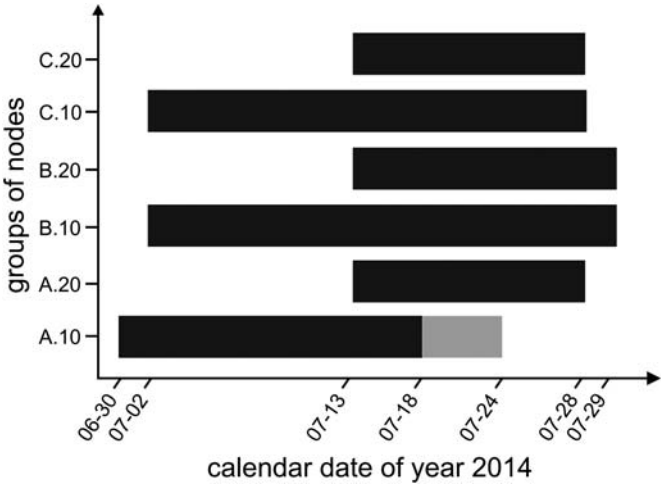

▲ **Figure 2.** Summary of the start and end times of groups of nodes (year 2014). Each grid point has two collocated nodes noted as ".10" and ".20." The gray rectangle corresponds to a period when all A.10 nodes were grouped together at one point of array A (possibly A.44).

frequencies in which we found to be suitable for beamforming with this array. Above 10 Hz, the PSD is extremely variable in time, and the PSD shows a much greater spread. Both the maximum and minimum noise levels in the band are different at each station, even for the very closely spaced stations at B33, and frequently peaked. When noise levels are similar at collocated stations, as they are in our band of interest from 1 to 10 Hz, it is necessary to perform a coherence analysis to properly assess the quality of the data. The PQLX analysis of the VolcArray data can be browsed remotely (contact geodata@ujf-grenoble.fr for more detail).

Figure 4 shows a coherence analysis for station B33. The total and noncoherent acceleration PSDs are plotted in Figure 4a, whereas the coherence itself is plotted (using a logarithmic scale) in Figure 4b. The noncoherent PSD is estimated using a modified version of the method of Holcomb (1989). Appendix A includes a discussion of the robustness of this estimator and the use of a logarithmic scale for coherence. An estimate of the self-noise of the FairfieldNodal ZLand 1C (FairfieldNodal, 2014) is plotted alongside the measured acceleration PSDs in Figure 4a. It was computed by converting the root mean square noise specification at the input by the square root of the expected digitizer bandwidth to obtain a PSD in counts per square root of frequency (counts per square root of hertz) and then referring this to units of ground motion by dividing by the nominal geophone transfer function. The agreement of the observed total noise PSD with this specification is very good in the 0.01–0.1 Hz band, validating the modeling and showing that instrument noise cannot explain the observed noncoherent noise over the rest of the band, from 0.1 to 100 Hz.

The flatness of the logarithmic coherence between 0.2 and 2 Hz, and consequently the similarity of shape of the total and noncoherent noise spectra in this band, suggests that the explanation of the noncoherent noise must be consistent with frequency independence. A likely explanation is physical misalignment to vertical between the sensors. The noncoherent noise N_H between two sensors that are physically misaligned by an angle θ will be proportional to that angle (in radians) and the ground motion H in the direction perpendicular to their direction of sensitivity and the plane of the angle between them, $N_H = \theta H$. Thus, the misalignment can be estimated from the coherence (γ) using $\theta = 10^{\gamma/20}$. In this case, a logarithmic coherence of approximately 16 dB corresponds to a misalignment angle of 9°.

Above 2 Hz, after we enter the band of frequencies useful for beamforming, the coherence at B33 in this particular time period begins to decay. The incoherence could be due to a number of effects, including locally coupled environmental (e.g., wind) noise or rotational ground motion combined with the sensors being imperfectly collocated. Regardless, the level of incoherence in a given band is a good indicator of the quality of data for beamforming in that band. Figure 5 summarizes the coherence across the subarrays in the band 2–6 Hz. Stations with more than 5 dB of coherence show as green in Figure 5 and can be unhesitatingly used in beamforming operations. Conversely, stations showing in red need further investigation.

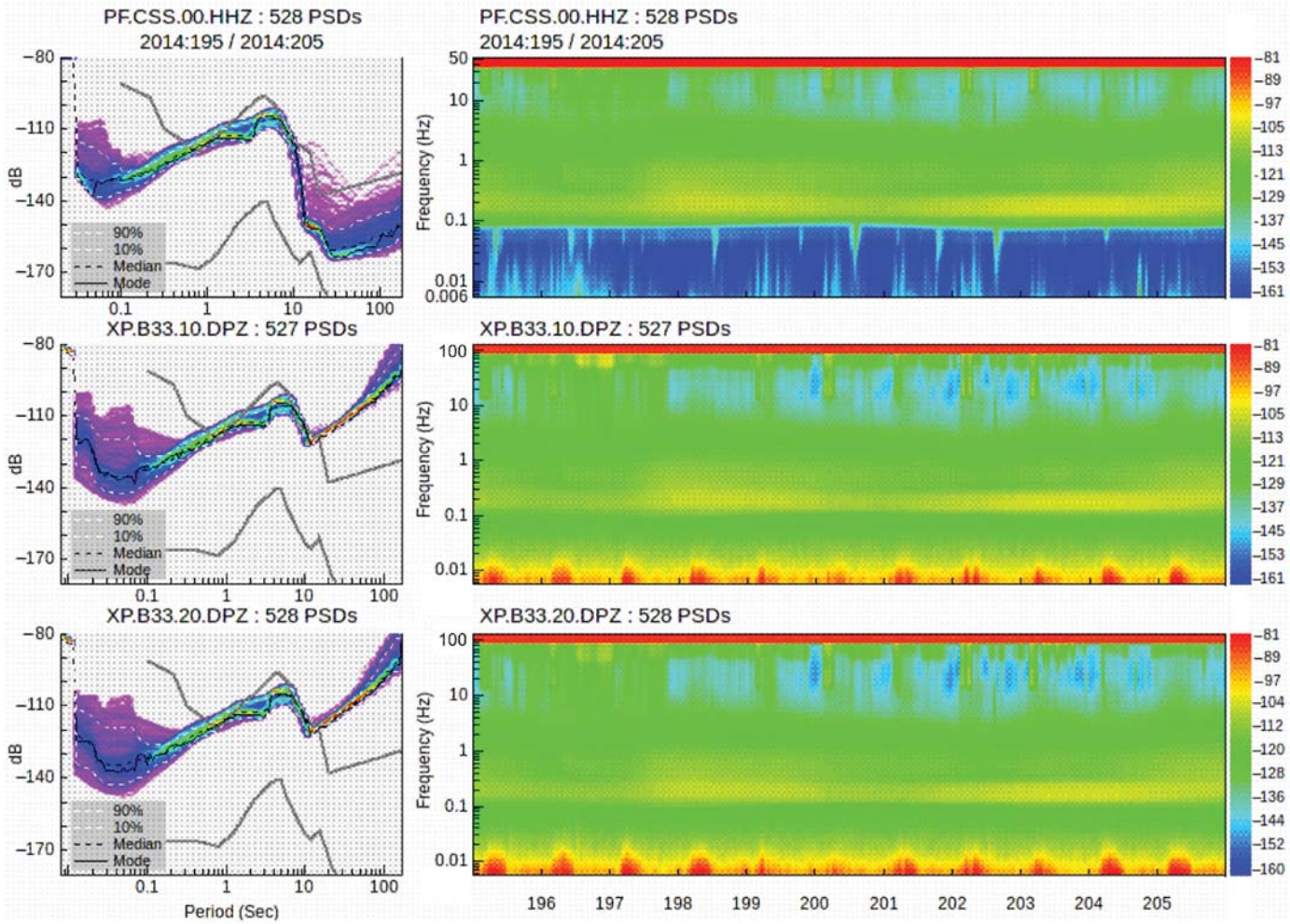

▲ **Figure 3.** PQLX spectral analysis results for the 11 days for which data were available at both VolcArray stations B33.10 (middle row) and B33.20 (bottom row), along with the broadband station CSS (top row). The time period spans Julian days 195–206, corresponding to the dates 14 July 2014 to 25 July 2014. The left column shows power spectral density (PSD) probability density functions. The right column shows the same data, in the form of a spectrogram. The units are acceleration PSD (dB with respect to $m^2/s^4/Hz$).

For the time period shown in Figure 5, for example, further investigation shows that station C27.10 appears to have moved beyond its tilt specification, so the output is effectively that which would be seen if the geophone mass was clamped or the input to the digitizer was terminated with a simple resistive load. The rest of the stations in red (A35, A43, A55, A57, and A66) were recording ground motion for this time period, but they have a logarithmic coherence greater than zero only at the microseismic peak, and even in that band they are not very coherent.

The time period chosen to assess data quality in Figures 4 and 5 was somewhat arbitrarily chosen at 2 hr. Welch's method gives a reduction in variance over long time periods; however, because it prescribes simple averaging of individual spectral estimates, it is also vulnerable to nonstationary noise sources, such that one outlier window can dominate the averaged result. Thus, shorter and more carefully chosen windows can result in lower estimates of both the total and noncoherent noise. In any case, when quantities such as cross correlation are to be computed on a windowed basis, it makes the most sense to assess coherence using the exact same windows. Cross correlations computed without temporal normalization on short, overlapping windows can give more rapid convergence than normalized cross correlations (Seats *et al.*, 2012); it may be that downweighting stations that are incoherent with their neighbors will further improve convergence.

In summary, for the studied time period (2 hr, starting at 14 July 2014 16:00 UTC) the data quality is, broadly speaking, best at subarray B and better at C than at A, although the uniformity of node placement is better at A than at C. No data are available for A16.20, B62.20, C41.20, and C44.10, whereas C27.10 is behaving as if the mass is clamped, so this station should be omitted from any analysis. Data quality at A35.10, A43.20, A55.20, A57.20, and A66.20 is generally poor, although there are time periods when those data should be usable. For the remaining stations, data quality is generally good, although it is time variable, and, for best results, it should be assessed on the fly during processing.

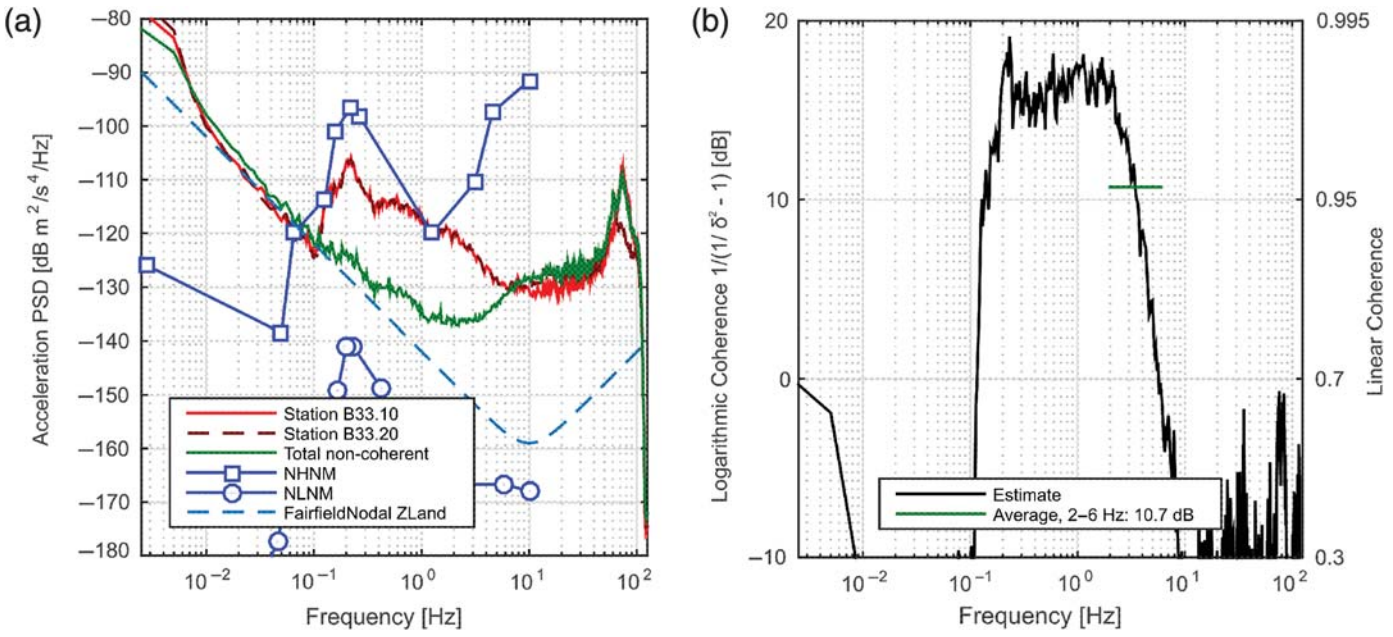

▲ **Figure 4.** Coherence analysis of VolcArray stations B33.10 and B33.20 for a 2 hr period starting at 14 July 2014 16:00 UTC. (a) Total PSD. The solid red line is the PSD for B33.10, and the dashed red line is for B33.20. The total noncoherent PSD (green) is estimated using a modified version of the method of Holcomb (1989). The new high-noise model and new low-noise model of Peterson (1993) are included for reference (blue, with markers). An estimate of the digitizer noise (blue dashed line), was computed using the nominal response and noise specification of the ZLand at 36 dB gain (FairfieldNodal, 2014). (b) Logarithmic coherence (black) for the same stations and time period. The average coherence (green) over the band 2–6 Hz.

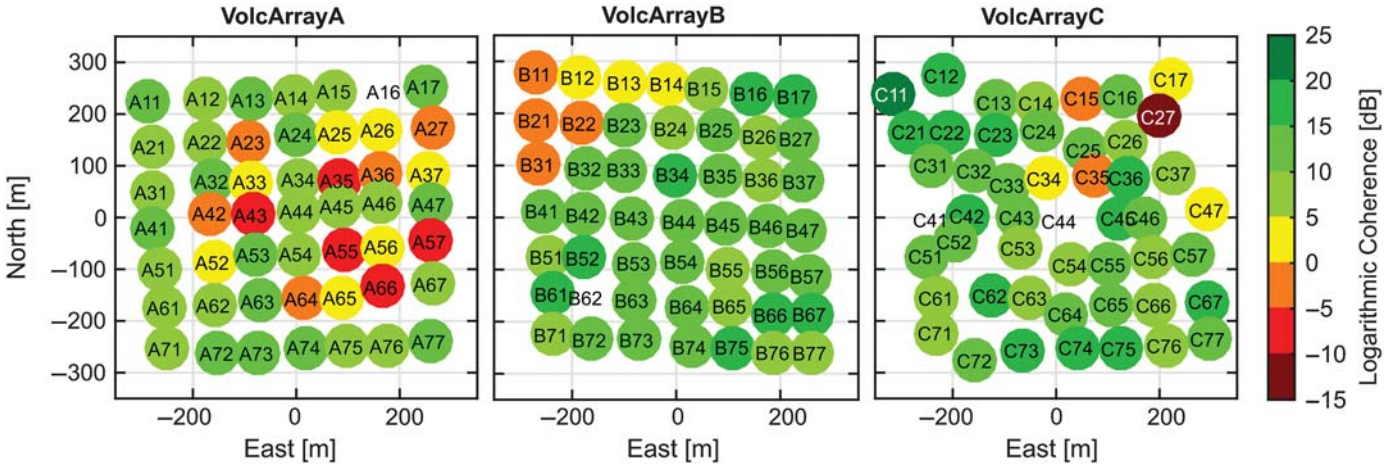

▲ **Figure 5.** Average coherence between 2 and 6 Hz for the stations in each subarray, for the same time period as Figure 4. Logarithmic coherences of 0, 10, and 20 dB correspond to coherences of approximately 0.7, 0.95, and 0.995, respectively. Coherence was not estimated at stations without circles, due to the unavailability of data from A16.20, B62.20, C41.20, and C44.10.

PROPERTIES OF RECORDED AMBIENT SEISMIC NOISE

Because our main goal is to reconstruct body waves from correlations of ambient seismic noise, we first study the noise properties using array processing. We apply a beamforming technique to the continuous seismic records to understand the directionality of the seismic wavefield energy. Beamforming is one of the classical techniques to analyze seismic waves and improve signal-to-noise ratio (Rost and Thomas, 2002). Here, we take advantage of the high density of each subarray to avoid aliasing issues and possibly to track body-wave sources; hence, we perform beamforming at each subarray separately.

We choose here to perform a plane wave beamforming that we implement in the time domain, similarly to a slant-stack technique. For each horizontal slowness vector, we first

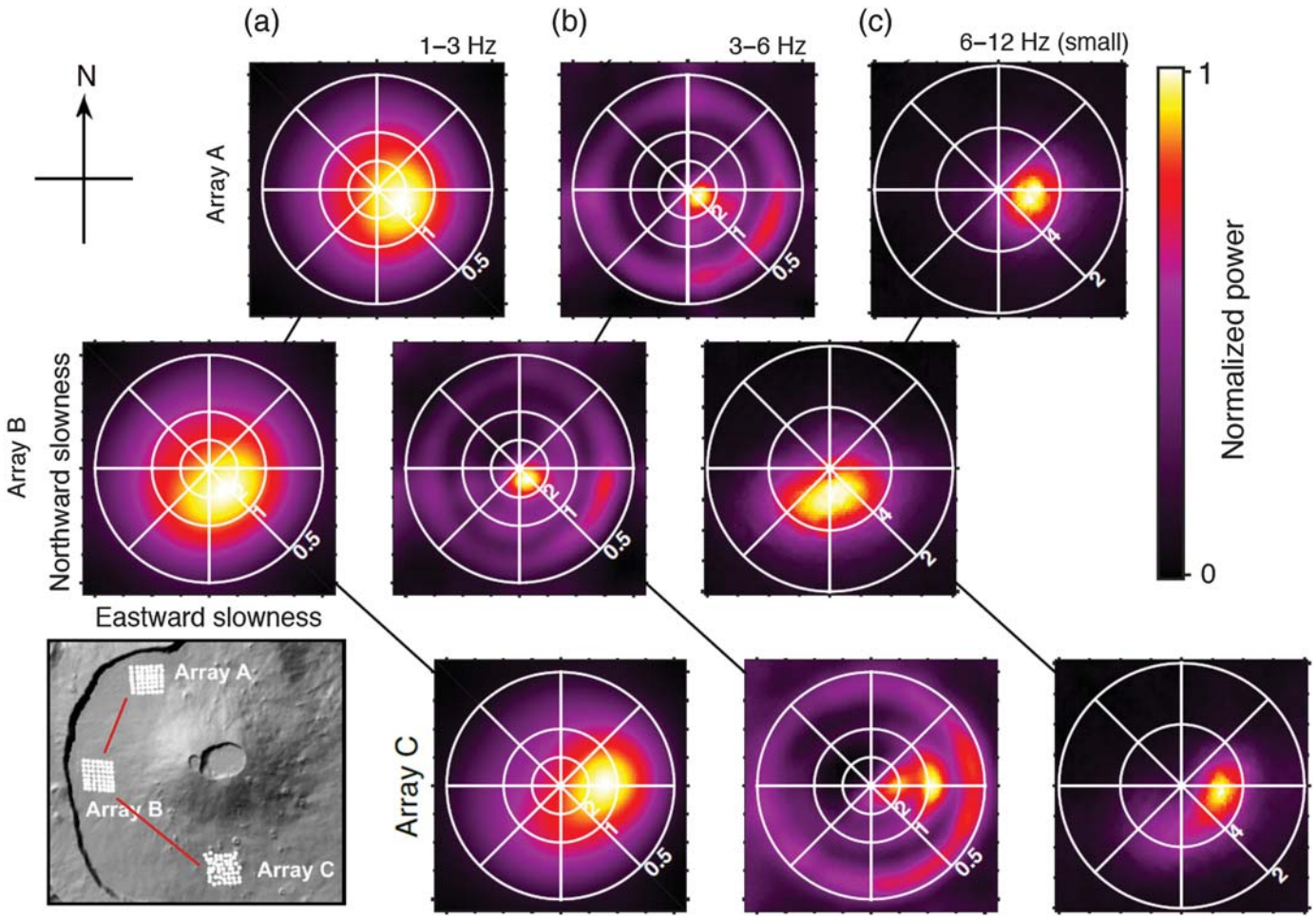

▲ **Figure 6.** Power of observed ambient noise at each array in the horizontal slowness domain averaged over the entire one-month recording. The power was computed in three different frequency bands: (a) 1–3 Hz, (b) 3–6 Hz, and (c) 6–12 Hz. A bright color indicates a direction of strong incoming energy; amplitudes are independently normalized at each panel. In each frequency band, panels are located at the relative location of each array (see the inset map) and connected by black lines. The numbers at each white circle indicate the corresponding velocity in kilometers per second. The scaling of slownesses in (c) is different from the other panels.

slant stack the ambient noise based on the distance from the central receiver. Then, we compute the envelope of stacked wavefields in each frequency range (1–3 Hz, 3–6 Hz, and 6–12 Hz here). Last, we compute the mean amplitude of the envelope at each frequency range. In Figure 6, we show the averaged beams over the entire deployment time (about 30 days with locations 10 and 20) at different frequencies.

At 1–3 Hz, the strong surface-wave energy comes from the southeast with velocity of about 1.0 km/s. At 3–6 Hz, we find both surface- and body-wave energies. Body waves propagate faster than 2 km/s, and surface waves propagate around 0.75 km/s. The body-wave velocity is an apparent velocity, because we are observing 3D wave propagation with a 2D array. Because Figure 6b shows bright rings around 0.75 km/s, the surface waves propagate from a variety of directions. The velocity of surface waves in array C is slower than other arrays, which is explained by the presence of a large number of recent lava flows in this area, which are relatively compliant. In the high-frequency range (Fig. 6c), we detect a strong spot of body waves with velocity of 5–6 km/s. Interestingly, the direction of incoming waves changes during the observation (see Appendix C for more detail). The origin of these incoming body waves is very likely related to ocean–seafloor interaction close to the coast of La Réunion. They could also find their origin in the propagation of acoustic waves in the SOund Fixing And Ranging (SOFAR) channel and their conversion to elastic waves along the flanks of La Réunion's underwater volcanic edifice.

The size of an array determines the resolution obtainable by beamforming; and, based on the synthetic test shown on Figure B1 (Appendix B), 1 Hz is about the lower limit for finding the direction of wavefields without deconvolving the array response (Rost and Thomas, 2002). To completely avoid aliasing effects given the average sensor spacing of 85 m, and assuming perfect plane-wave propagation at or above 0.75 km/s in the vicinity of the array, the upper limit for frequency would be $f_{\max} = c_{\min}/(2\Delta x) = 4.4$ Hz. However, we demonstrate in Figures 6 and B1 that the highest frequency

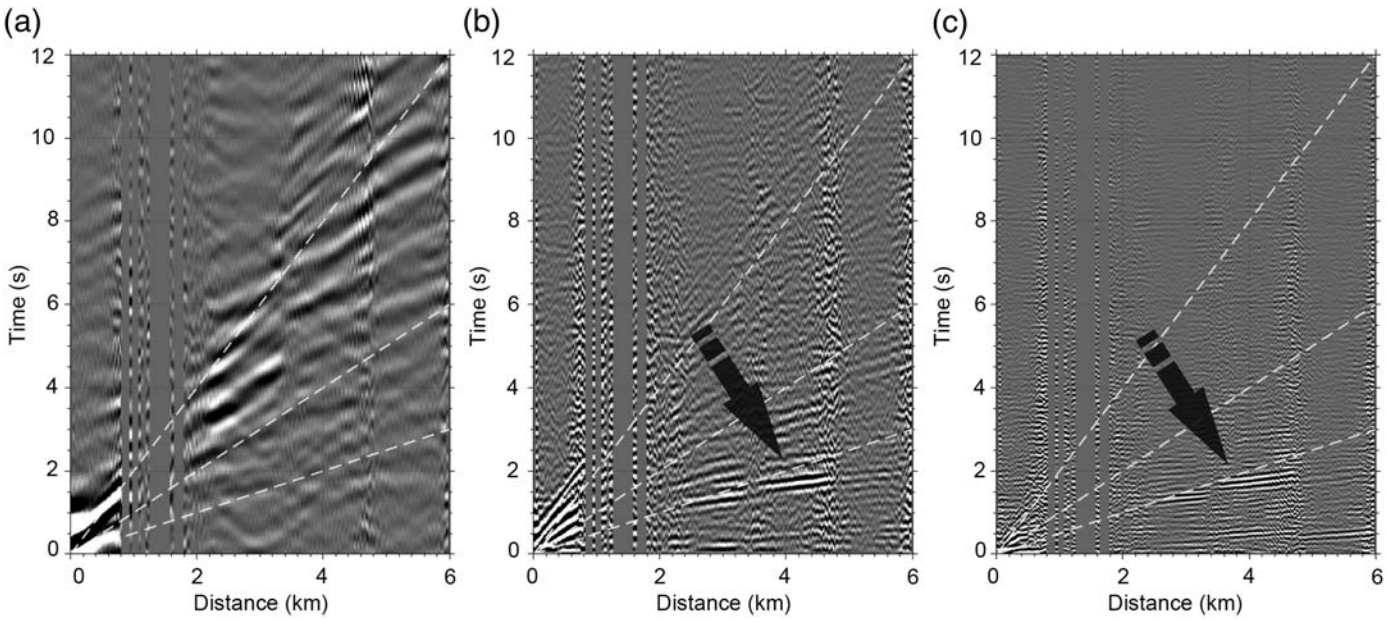

▲ **Figure 7.** Correlation functions in (a) 1–3 Hz, (b) 3–6 Hz, and (c) 6–12 Hz. The white lines illustrate the arrival times of waves with apparent velocities of 2, 1, and 0.5 km/s. Black arrows point toward possible reconstructed direct *P* waves traveling between arrays.

band is not contaminated by aliasing by showing continuity of wave energy from low to high frequency. In particular; the surface waves dominant in the 1–3 Hz band and the body waves dominant in the 6–12 Hz band are separately resolvable in the 3–6 Hz band.

DISCUSSION AND CONCLUSION

The noise beamforming results are encouraging because they show a high content of body waves at frequencies between 3 and 12 Hz. Our main interest is, however, to be able to reconstruct direct and scattered body waves between arrays, especially between arrays A and C. Indeed, this would allow us to extract information from waves directly probing the vicinity of the active magma reservoir below the central active crater. To this end, we cross correlate observed ambient noise at each receiver pair and plot all correlations as a function of the distance between receivers (Fig. 7). We find clear low-velocity waves at lower frequencies (1–3 Hz, Fig. 7a) that very likely correspond to surface waves. Interestingly, at higher frequencies (3–6 and 6–12 Hz, Fig. 7b,c), we find coherent energy at high velocities around 2 km/s. Considering that, at these frequencies, body waves dominate ambient seismic noise records (Fig. 6), we believe that this coherent energy corresponds to body waves. However, the question remains: are these really body waves from the Green's functions between arrays or does this body-wave energy come from the correlation of the strong source signal of body waves detected in Figure 6? To answer this difficult question, we performed a double beamforming (Boué *et al.*, 2013) study that helps to decipher the azimuth and apparent velocities of the reconstructed waves shown in Figure 7. These results are described in a companion article (N. Nakata *et al.*, unpublished manuscript, 2015). By extracting direct and possibly scattered body waves traveling through the active core of volcanoes, we expect to open the way to 4D imaging and monitoring of active volcanoes and possibly also seismic faults.

DATA AND RESOURCES

The data and metadata are available without restrictions from the Réseau sismologique and géodésique français (RESIF) and European Integrated Data Archive (EIDA) datacenters (www.resif.fr, http://www.orfeus-eu.org/eida/) under the International Federation of Digital Seismograph Networks (FDSN) network code XP (doi: 10.15778/RESIF.XP2014). The VolcArray XP dataset consists of about 500 GB of miniSEED data (32-bit floating point) for 152 stations or grid points, most of them having two streams (location codes .10 and .20 for collocated nodes).

Data and metadata can be retrieved using (1) http and standard FDSN webservices station and dataselect and any http client (wget, curl, obspy clients,...), (2) ArcLink EIDA protocol and dedicated clients (arclink_fetch, obspy clients, ...), or (3) *rsync* protocol. *Rsync* should be used for downloading the whole dataset of continuous data. Other data services are more suitable for targeted data requests (time-windowed, quality-filtered, etc.) of smaller amounts of data. Examples and guidelines about data and metadata retrieval can be found on http://portal.resif.fr/?-Accessing-data- and http://ws.resif.fr. All above websites are last accessed on October 2015. The unpublished manuscript by N. Nakata, P. Boué, F. Brenguier, P. Roux, and M. Campillo, "Body- and surface-wave reconstruction from seismic noise correlations between arrays at Piton de la Fournaise volcano," *Geophys. Res. Lett.*

ACKNOWLEDGMENTS

VolcArray is a joint project between ISTerre, Observatoire Volcanologique du Piton de la Fournaise (OVPF), Institut de Physique du Globe de Paris (IPGP), and Parc National de La Réunion. It was funded by Institut de France (prix Del Duca), La ville de Paris (projet Emergences), the Russian Science Foundation (Grant 14-47-00002) and the Service National d'Observation en Volcanologie with support from FairFieldNodal company. The data were prepared and are distributed by RESIF/temporary networks. We acknowledge the editor and the two reviewers for providing us with valuable comments that greatly improved the manuscript.

REFERENCES

Bendat, J. S., and A. G. Piersol (2011). *Random Data: Analysis and Measurement Procedures*, Fourth Ed., John Wiley & Sons, Hoboken, New Jersey.

Beyreuther, M., R. Barsch, L. Krischer, T. Megies, Y. Behr, and J. Wassermann (2010). ObsPy: A Python toolbox for seismology, *Seismol. Res. Lett.* **81,** no. 3, 530–533.

Boué, P., P. Roux, M. Campillo, and B. de Cacqueray (2013). Double beamforming processing in a seismic prospecting context, *Geophysics* **78,** no. 3, V101–V108.

Brenguier, F., M. Campillo, T. Takeda, Y. Aoki, N. M. Shapiro, X. Briand, K. Emoto, and H. Miyake (2014). Mapping pressurized volcanic fluids from induced crustal seismic velocity drops, *Science* **345,** no. 6192, 80–82.

Brenguier, F., P. Kowalski, T. Staudacher, V. Ferrazzini, F. Lauret, P. Boissier, P. Catherine, A. Lemarchand, C. Pequegnat, O. Meric, *et al.* (2012). First results from the UnderVolc high resolution seismic and GPS network deployed on Piton de la Fournaise volcano, *Seismol. Res. Lett.* **83,** no. 1, 97–102.

Brenguier, F., N. M. Shapiro, M. Campillo, V. Ferrazzini, Z. Duputel, O. Coutant, and A. Nercessian (2008). Towards forecasting volcanic eruptions using seismic noise, *Nature Geosci.* **1,** no. 2, 126–130.

Brenguier, F., N. M. Shapiro, M. Campillo, A. Nercessian, and V. Ferrazzini (2007). 3-D surface wave tomography of the Piton de la Fournaise volcano using seismic noise correlations, *Geophys. Res. Lett.* **34,** no. 2, L02305, doi: 10.1029/2006GL028586.

Evans, J. R., F. Followill, C. R. Hutt, R. Kromer, R. L. Nigbor, A. Ringler, J. Steim, and E. Wielandt (2010). Method for calculating self-noise spectra and operating ranges for seismographic inertial sensors and recorders, *Seismol. Res. Lett.* **81,** no. 4, 640–646.

FairfieldNodal (2014). ZLand 1C specifications, http://www.fairfieldnodal.com/assets/media/pdf/Zland-1C-specs.pdf (last accessed March 2015).

Hand, E. (2014). A boom in boomless seismology, *Science* **345,** no. 6198, 720–721.

Holcomb, L. G. (1989). A direct method for calculating instrument noise levels in side-by-side seismometer evaluations, *U.S. Geol. Surv. Open-File Rept. 89-214.*

Holcomb, L. G. (1990). A numerical study of some potential sources of error in side-by-side seismometer evaluations, *U.S. Geol. Surv. Open-File Rept. 90-406.*

Jaxybulatov, K., N. M. Shapiro, I. Koulakov, A. Mordret, M. Landès, and C. Sens-Schönfelder (2014). A large magmatic sill complex beneath the Toba caldera, *Science* **346,** no. 6209, 617–619.

McNamara, D. E., and R. P. Buland (2004). Ambient noise levels in the continental United States, *Bull. Seismol. Soc. Am.* **94,** no. 4, 1517–1527.

Nakata, N., J. P. Chang, J. F. Lawrence, and P. Boué (2015). Body wave extraction and tomography at Long Beach, California, with ambient-noise interferometry, *J. Geophys. Res.* **120,** 1159–1173, doi: 10.1002/2015JB011870.

Obermann, A., T. Planes, E. Larose, and M. Campillo (2013). Imaging pre- and co-eruptive structural changes of a volcano with ambient seismic noise, *J. Geophys. Res.* **118,** 6285–6294.

Peterson, J. (1993). Observations and modeling of seismic background noise, *U.S. Geol. Surv. Open-File Rept. 93-322.*

Rivet, D., F. Brenguier, and F. Cappa (2015). Improved detection of preeruptive seismic velocity drops at the Piton de La Fournaise volcano, *Geophys. Res. Lett.* **42,** 6332–6339, doi: 10.1002/2015GL064835.

Rost, S., and C. Thomas (2002). Array seismology: Methods and applications, *Rev. Geophys.* **40,** no. 3, 2-1–2-27.

Roux, P., K. Sabra, P. Gerstoft, and W. Kuperman (2005). *P*-waves from cross-correlation of seismic noise, *Geophys. Res. Lett.* **32,** no. 19, L19303.

Roux, P., M. Wathelet, and A. Roueff (2011). The San Andreas fault revisited through seismic noise and surface wave tomography, *Geophys. Res. Lett.* **38,** L13319, doi: 10.1029/2011GL047811.

Seats, K. J., J. F. Lawrence, and G. A. Prieto (2012). Improved ambient noise correlation functions using Welch's method, *Geophys. J. Int.* **188,** no. 2, 513–523.

Sens-Schönfelder, C., and U. Wegler (2006). Passive image interferometry and seasonal variations of seismic velocities at Merapi Volcano, Indonesia, *Geophys. Res. Lett.* **33,** no. 21, L21302.

Shapiro, N. M., M. Campillo, L. Stehly, and M. H. Ritzwoller (2005). High-resolution surface-wave tomography from ambient seismic noise, *Science* **307,** no. 5715, 1615–1618.

Sleeman, R., A. Van Wettum, and J. Trampert (2006). Three-channel correlation analysis: A new technique to measure instrumental noise of digitizers and seismic sensors, *Bull. Seismol. Soc. Am.* **96,** no. 1, 258–271.

APPENDIX A

ESTIMATES OF NONCOHERENT NOISE FROM TWO COLLOCATED SENSORS

When three or more collocated sensors are available, the self-noise of each sensor can be separately estimated (Sleeman *et al.*, 2006). When only two sensors are available, their individual contributions can be isolated using the method of Holcomb (1989) but only to the extent that the sensor transfer functions are precisely and accurately known (Holcomb, 1990). Holcomb's method breaks down for even moderate levels of signal to noise and thus coherence. On the other hand, if it is accepted, in the two-sensor case, that the self-noise of the individual sensors cannot be separated, then it becomes possible to extend Holcomb's method in such a way as to estimate the total noncoherent noise without such exact knowledge.

Neglecting the effect of transfer functions, assuming stationarity and omitting frequency dependence of all quantities, the complex spectrum at the output of the jth sensor, S_j is related to the input signal X and its self-noise by $S_j = X + N_j$. Because the input signal and self-noise are uncorrelated, the expectation values of the autospectra and cross spectra are

$$P_{jj} = |X|^2 + |N_j|^2 \tag{A1}$$

and

$$P_{jk} = |X|^2. \tag{A2}$$

The essence of Holcomb's method is then to compute

$$|N_j|^2 = P_{jj} - P_{jk} \tag{A3}$$

by estimating the expectation value of the auto- and cross-spectral densities using a suitable method such as Welch's method. In practice, this works well enough for low signal-to-noise ratios, but at high signal to noise the accuracy is severely impaired by insufficient knowledge of the exact transfer functions of the sensors (Holcomb, 1989, 1990; Evans *et al.*, 2010).

The coherence of the outputs is defined as $\gamma_{jk}^2 \equiv |P_{jk}|^2/(P_{jj}P_{kk})$. It follows from equations (A1) and (A2) that

$$\gamma_{jk}^2 = \frac{1}{\left(1+\frac{|N_j|^2}{|X|^2}\right)\left(1+\frac{|N_k|^2}{|X|^2}\right)}. \tag{A4}$$

For high coherence, the expectation value of the coherence is therefore well approximated by

$$\gamma_{jk}^2 \approx \frac{1}{1+\frac{|N_j|^2+|N_k|^2}{|X|^2}}. \tag{A5}$$

Thus, we can obtain a reliable estimate of the sum of the noncoherent noise of the individual sensors by treating high- and low-coherence cases differently:

$$|N_j|^2 + |N_k|^2 \approx \begin{cases} |P_{jk}|/(1/\gamma_{jk}^2 - 1), & \gamma \geq 0.9 \\ P_{jj} + P_{kk} - 2|P_{jk}|, & \gamma < 0.9 \end{cases}. \tag{A6}$$

The threshold for distinguishing the two cases is not critical; in practice $\gamma \geq 0.9$ for identifying the high-coherence case works well.

In the low-coherence case, the estimate is good because it is easy to obtain sufficiently accurate estimates of the correct transfer functions. In the high-coherence case, the estimate is good because we can neglect a term in $|N_j|^2|N_k|^2/|X|^4$; in fact, in this case the coherence gives us an estimate of the signal-to-noise power ratio.

Rather than plotting coherence on a linear scale, as is customary, it can be more expressive to plot the logarithmic coherence in dB as shown in Figure 4b, using $\gamma_{\mathrm{dB}} = -10\log_{10}(1/\gamma_{jk}^2 - 1)$. This effectively takes the linear coherence, which spans the unit interval, and maps it to the whole set of real numbers, from $-\infty$ to ∞. By way of comparison, log-

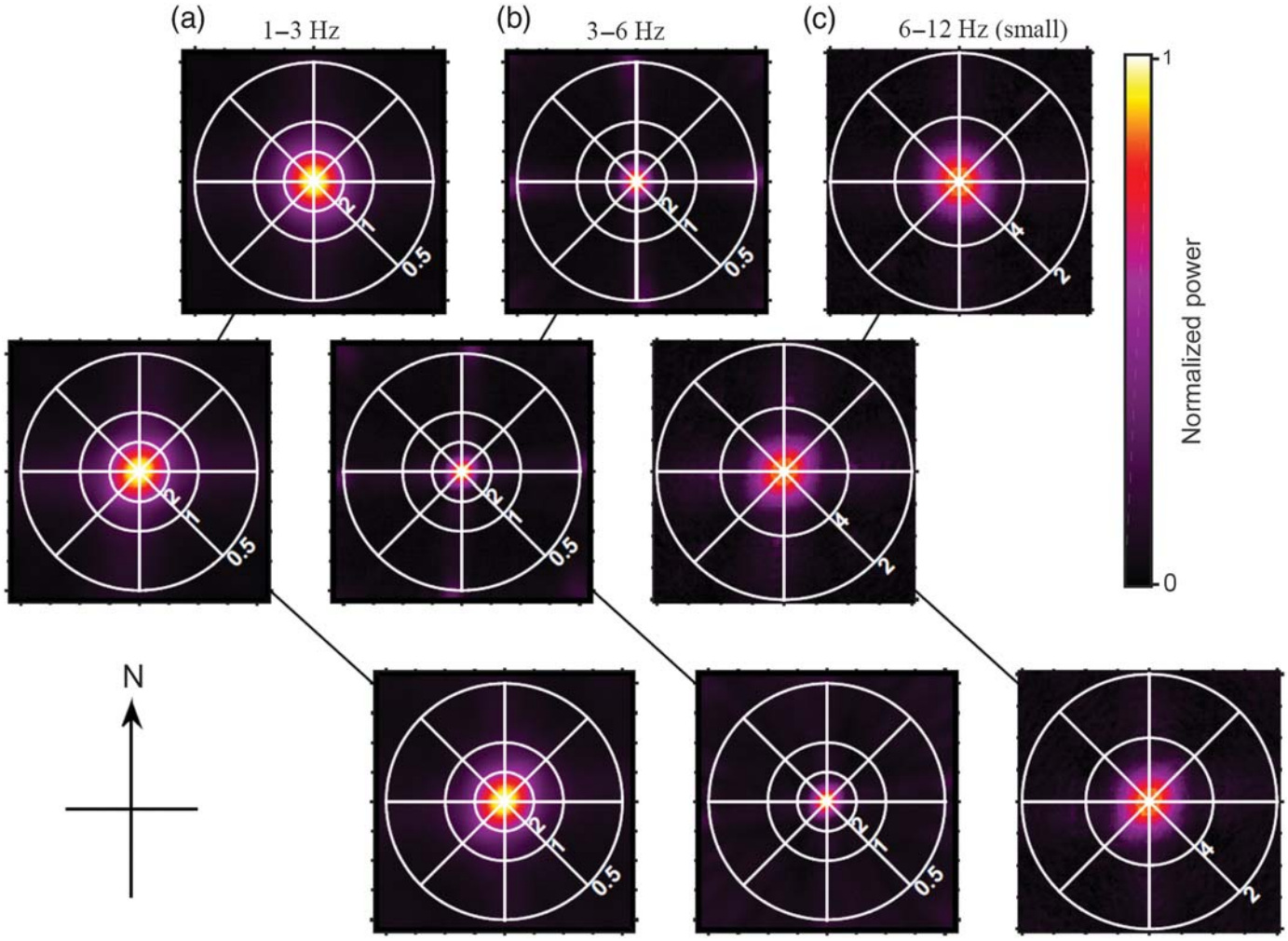

▲ **Figure B1.** Frequency-slowness responses of the arrays in a similar representation as for Figure 6.

arithmic coherences of 0, 10, and 20 dB correspond to (linear) coherences of approximately 0.7, 0.95, and 0.995, respectively.

It is instructive that this same quantity (the inverse squared coherence minus one) is instrumental to estimating the error in estimates of other parameters, for example, the error in an estimate of the relative transfer function $|\hat{H}_{jk}| = |P_{jk}/P_{jj}|$ in the presence of stationary Gaussian noise. In this case, the normalized random error in the transfer function estimate is $\varepsilon^2 = (1/\gamma_{jk}^2 - 1)/2N$, in which N is the number of independent windows stacked in producing the estimate (Bendat and Piersol, 2011).

APPENDIX B

FREQUENCY–SLOWNESS RESPONSES OF THE ARRAYS

To assess the resolution and accuracy of the beamforming results shown in Figure 6, we computed the frequency–slowness response of the arrays. Figure B1 shows this response in a similar representation as for Figure 6. For this test, the input is a synthetic monochromatic function with the same phase at each array point (i.e., vertical incident synthetic sine wave). Each panel corresponds to a linear averaging over each frequency range of individual frequencies beamforming outputs. This test highlights that the different type of waves described on Figure 6 are well resolved.

APPENDIX C

TEMPORAL EVOLUTION OF NOISE PROPERTIES

To understand the origin of the dominant noise signal described in Figure 6, it is interesting to analyze the temporal evolution of the amplitude and azimuth of these dominant waves. Figure C1 shows the amplitude and azimuth of observed peak signal power after beamforming over time for each array. First, we can observe that for low frequencies (0.5–1 Hz) where the microseismic surface waves dominate, the azimuth of

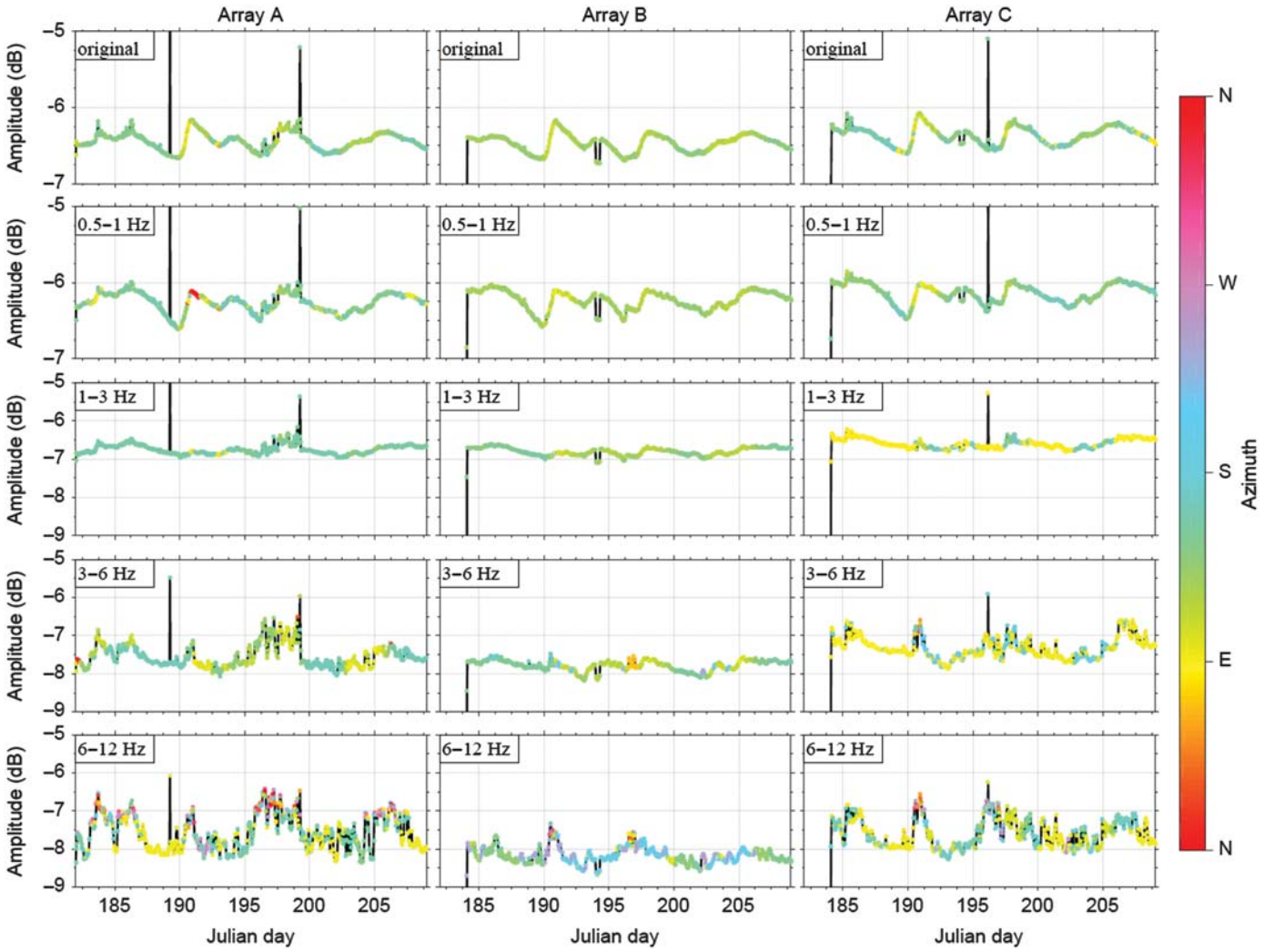

▲ **Figure C1.** Amplitude and azimuth of observed peak signal power after beamforming. Each column corresponds to an array, whereas each row corresponds to a different frequency band, as indicated. Original means the observed data without applying any band-pass filter.

incoming waves is quite stable with a preferential southeastward direction. This direction relates with the origin of the main storms in this region, which mostly occur in the southern Indian Ocean. At higher frequencies where the body waves dominate (6–12 Hz), the amplitude and azimuth distribution is more scattered in time and does not perfectly match with the low frequencies. In conclusion, even though the main mechanisms of production of surface and body waves seems similar (preferential a southeastern direction), the origin of high-frequency body waves seems more complex with possibly different mechanisms acting together at the same time (swell–ocean floor interaction, wind interaction with surface ground, acoustic waves propagating in the SOFAR channel converted on the island flanks underwater).

F. Brenguier
N. Ackerley
M. Campillo
E. Larose
C. Pequegnat
P. Roux
J. Chaput
Institut des Sciences de la Terre
Université Grenoble Alpes, CNRS
BP 53
38041 Grenoble CEDEX 9
France
florent.brenguier@ujf-grenoble.fr

P. Kowalski
V. Ferrazzini
N. Villeneuve
Observatoire Volcanologique du Piton de la Fournaise
Institut de Physique du Globe de Paris
Sorbonne Paris Cité, CNRS
14 RN3, Km 27
97418 La Plaine des Cafres
Réunion, France

N. Nakata
P. Boué
Stanford University
397 Panama Mall
Stanford, California 94305 U.S.A.

S. Rambaud
FairFieldNodal
1111 Gillingham Lane
Sugar Land, Texas 77478 U.S.A.

T. Lecocq
Observatoire Royal de Belgique
Section de Séismologie
Avenue Circulaire, 3
1180 Bruxelles, Belgium

N. M. Shapiro
Institut de Physique du Globe de Paris
Sorbonne Paris Cité, CNRS
1, rue Jussieu
75238 Paris CEDEX 05
France

Published Online 25 November 2015